Scientific Research Publishing

Energy and Power Engineering, 2023, 15, 372-398
https://www.scirp.org/journal/epe
ISSN Online: 1947-3818
ISSN Print: 1949-243X

# Powering a Low Power Wireless Sensor in a Harsh Industrial Environment: Energy Recovery with a Thermoelectric Generator and Storage on Supercapacitors

**Vincent Boitier[1,2], Bruno Estibals[1,2], Lionel Seguier[1]**

[1]Laboratoire d'Analyse et d'Architecture des Systèmes—Centre National de la Recherche Scientifique, Université de Toulouse, Toulouse, France
[2]Université Paul Sabatier, Toulouse, France
Email: vincent.boitier@laas.fr

**How to cite this paper:** Boitier, V., Estibals, B. and Seguier, L. (2023) Powering a Low Power Wireless Sensor in a Harsh Industrial Environment: Energy Recovery with a Thermoelectric Generator and Storage on Supercapacitors. *Energy and Power Engineering*, **15**, 372-398.
https://doi.org/10.4236/epe.2023.1511022

**Received:** June 28, 2023
**Accepted:** November 17, 2023
**Published:** November 20, 2023



## Abstract

Wireless sensor networks are widely used for monitoring in remote areas. They mainly consist of wireless sensor nodes, which are usually powered by batteries with limited capacity, but are expected to last for long periods of time. To overcome these limitations and achieve perpetual autonomy, an energy harvesting technique using a thermoelectric generator (*TEG*) coupled with storage on supercapacitors is proposed. The originality of the work lies in the presentation of a maintenance-free, robust, and tested solution, well adapted to a harsh industrial context with a permanent temperature gradient. The harvesting part, which is attached to the hot spot in a few seconds using magnets, can withstand temperatures of 200˚C. The storage unit, which contains the electronics and supercapacitors, operates at temperatures of up to 80˚C. More specifically, this article describes the final design of a 3.3 V 60 mA battery-free power supply. An analysis of the thermal potential and the electrical power that can be recovered is presented, followed by the design of the main electronic stages: energy recovery using a BQ25504, storage on supercapacitors and finally shaping the output voltage with a boost (*TPS*610995) followed by an LDO (*TPS*71533).

## Keywords

Energy Recovery, Battery-Free System, Supercapacitor, Thermoelectric Generator, TEG, BQ25504, Energy Management, Thermal Gradient

## 1. Introduction

Improving industrial processes requires increased monitoring of installations, with many sensors strategically deployed.

The 2idO project [1] (*IoT in an industrial environment*) has highlighted a demand from manufacturers for a complete autonomous sensor node (sensor, processing, radio, and power supply) in the size of a cigarette packet ($10 \times 7 \times 4$ $cm^3$) for a maximum price of €50 and capable of operating for more than a decade under variable environmental conditions.

In this paper, we focus on the power supply to such a sensor node when a hard-wired supply is not possible (*deployment is too costly*; the *area is unsuitable for cable routing*). In this case, one of the biggest challenges is the battery lifetime. In some applications, the amount of embedded energy and the weight and volume of the battery required to cover the expected lifetime of the product would be too large or too costly to meet the specifications expressed. Replacing the batteries after a certain period may be considered but is not always appropriate. In fact, the cost of exchanging batteries in hundreds of devices, especially if they are in hard-to-reach or hazardous locations, can make the entire network deployment cost-prohibitive [2].

An alternative solution we are considering is to harvest the available energy in the device's environment. Based on the conversion of ambient energy into electrical power, this approach has the potential to make IoT devices maintenance-free and permanently powered [3] [4]. In this case, the sensor node must include an energy storage block which provides the output power despite the intermittency and possible variations of the ambient available energy.

Many commercial energy recovery solutions based on photovoltaic cells have been developed. It is more complicated to find off-the-shelf products that use thermo-electric generation as a source of electrical power. In this case, the power supply of the sensor node needs to be fully dimensioned according to the thermal potential and the consumption profile, and it is the purpose of the paper.

The installation of a vibration sensor in the environment of a Total refinery in Gonfreville, France, offers a concrete and interesting use case for a thermoelectric energy harvester as a hot area is very close to the monitored engine.

Based on the operating requirements and the environmental conditions coming from the use case, this article highlights the rules that need to be considered in terms of TEG, electronics and storage for successful sizing and explains some of the pitfalls to be avoided.

After a literature review on TEG applications, a global presentation of the chosen electronic structure is exhibited. The analysis of the thermal potential is conducted, in the way to modelling and sizing both the TEG and its heatsink. Then, the electronic unit is detailed: extraction circuit, storage stage and regulation of the output voltage. A validating part is realized before the industrial deployment. A conclusion ends the paper.

## 2. Literature Review

Thermo-electro-generation (*the conversion of a heat stream into electricity*) offers several advantages: no moving parts, long service life and silent operation. Thermoelectric generators (*TEGs*) therefore have many potential applications [5]. TEGs are used in many applications such as automotive engines [6], industrial electronics [7], micro self-powered wireless platforms [8], health monitoring [9], tracking systems and aerospace [10]. These applications require different sizes and power supplies.

Terrestrial systems can be divided into several areas [11] depending on the temperature gradient and therefore the available electrical power.

The first class of applications is aimed at recovering large quantities of waste heat from industrial systems or from motor vehicles (*exhaust pipes*) and converting some of it into electrical power (*target between* 100 $W$ *and* 1 $kW$). But there are many challenges to overcome before commercial applications are available: price, low TEG efficiency (*a few percent*), heat extraction problems, expansion, non-uniform temperature field, and so on [12].

Another class of applications involves supplying power to very low-power wireless sensors for medical applications or wearables. The thermal gradients available are low on humans or animals ($\Delta T \approx 10^{\circ}\mathrm{C}$) and the constraints of mass and volume are significant. The electrical power recovered remains low (*between* 1 *and* 100 $\mu W$) [13] [14].

Finally, there is a third class of applications in which we are interested in dedicated to powering wireless sensors for monitoring and preventive maintenance applications in industrial environments, with electrical powers to be recovered of between 1mW and a few Watt, and numerous constraints: weight, volume, safety. Thermal gradients can be significant ($\Delta T > 60^{\circ}\mathrm{C}$), which is favorable to good recovery, but there are also sometimes severe constraints on the temperature on the hot side ($T_{HOT} > 200^{\circ}\mathrm{C}$) and sometimes a great temperature variability over time.

Some completed industrial products (*including the TEG harvester and power conversion stage*) are available. Generally, the harvesting TEG solution is an option on a wireless sensor initially powered by wires batteries, or supercapacitors [15]. In most cases, the energy recovery part is separate from the electronics part, but a monobloc design is possible, as presented by the start-up Moïz [16]. The tolerable high temperature is not specified here. The choice of an elegant monobloc solution depends on the maximum temperature of the hot source where the system will be installed. Such a solution is possible only if this maximum temperature can be supported by the electronic and storage components and will be avoided for our application. In addition, we notice that when the heatsink volume exceeds $\approx 1000\ \mathrm{cm}^3$, a multi-element design is preferred.

All products include a heat sink with the TEG, but some products, deliver enough power for supplying a radio or recharging a mobile phone and use a self-powered fan to promote the thermal gradient [17]. It significantly increases the harvested power, but if the fan stops, the TEG may be destroyed. Indeed, a

major problem is never to exceed the high temperature accepted by the TEG, on pain of destruction as explained in the notice of a TecTEG produce [18]. The need for a robust design eliminates this option in our study case.

Different situations are possible, with different gradients and therefore more or less recoverable electrical power, as shown in the examples below.

Thus, the difference between sewage water temperature and ambient air may be convenient (*between* –5˚C *and* 5˚C) for generating few power (60 $\mu W$) [19], but it is difficult to estimate the thermal potential because environmental conditions vary so widely. Generally, the air/water gradient remains low (*a few* ˚C) and can be used only for powering ultra-low-power applications [20]. The temperature gradient between near-surface soil and ambient air can also be used (*simulation paper*), but here again the recoverable power is less than 1mW in the best configuration [21].

Some interesting publications use a volume of a phase change material (*PCM*) placed on one side of the TEG, with the other side of the TEG connected to the ambient temperature. Using daily variations in ambient air temperature, this creates a temperature shift between the two sides of the TEG. So, the publication [22] shows an improvement of a factor of 6 between the solution with and without PCM material (*harvested power* ≈ 0.8 $mW$, 60 $J/day$). On the other hand, publication [23] presents much less interesting results: the maximum output power and the storable energy in the capacitor are 30 µW and 500 mJ.

For the above applications, the temperature levels (<40˚C) allow a monobloc design including the recharging system, battery, and electronics. This is not the case where there is a very hot spot, such as in automotive applications with for example a TEG located on an exhaust pipe [24] or for applications with burned gas [25]. In such cases, the high thermal gradient provides a significant level of power but means that the electronics and storage must be moved away from the hot zone. It should be noted in this latest cited publication that the loss of power due to clogging of the heat sink fins must not be neglected. It leads to a significant drop in power and could be problematic for maintenance-free systems.

Predicting the gradient and the air flow around the heat sink is a complex task. In an application of thermoelectricity using a stove, the authors show that the difference between the measured and predicted temperature can reach 50˚C depending on the localization [26]. This demonstrates the need for on-site measurements in complex environments.

To achieve significant electrical power, literature shows that the heatsink volume must be large enough to maintain the thermal gradient. This is a major drawback for mobile applications, but it is acceptable for industrial environments.

This literature review has shown us that it is easier to size a system in which the electronics and storage are placed (*along with the sensor and radio stage*) at a reasonable distance from the hot spot. The TEG should be chosen to withstand the maximum temperature level on the hot side. A suitable heatsink will be associated with the TEG to maintain a thermal gradient and therefore sufficient elec-

trical power. Finally, we can see from these readings that significant margins are necessary when sizing the energy recovery unit to take account of possible variations in the environmental conditions and modelling uncertainties.

## 3. Structure Overview

In general, an energy converter will not directly power a sensor, as the energy levels are too low, in the wrong form or not available at the right time. Therefore, a dedicated electronic circuit is required to provide intelligent power management. Figure 1 presents an overview of the power conversion chain used. It converts a part of the heat flux into electricity using a thermoelectric generator, stores it in supercapacitors and finally adapts the voltage to the level required by the load.

Secondary batteries are often used for energy storage. However, for an additional cost of around €15, replacing batteries with ultracapacitors (*because of their cycling and temperature performance*) is an interesting alternative for industrial products dedicated to IoT.

## 4. Thermoelectric Energy Generators (*TEGs*)

### 4.1. Introduction and Basis of Thermal Potential Evaluation

A thermoelectric generator (TEG) consists of an assembly of several tens or hundreds of pairs of thermocouples (TC) sandwiched between ceramic plates (Figure 2). All thermocouples are connected electrically in series and thermally in parallel. A part of the heat flow passing through the thermocouples is converted into electricity [22] [27] [28].

While the consumption of a sensor or collector node is predictable, the potential for thermal electrical energy is more difficult to estimate prior to installation. The first step in developing a TEG design is to study the heat source. This can be done using two possibilities:

- by energy and/or exergy analysis, carried out considering the recovery technology, *i.e.*, the thermoelectric devices [10],

- by On-site measurements [29].

We decided to use the second method, which is implemented in a petrochemical plant (*Total Gonfreville*, *France*) (Figure 3). For this purpose, a non-contact method of infrared thermal imaging technology allows us to show the variations in surface temperature and to detect potential thermal hazards. The thermal images were taken with a FLIR i60 thermal camera, limited to 150˚C in the mode used.

The technical specifications of the FLIR i60 are listed in Table 1.

The temperature is then measured using a Fluke 54 II B thermometer and two K TME thermocouple probes: a KS07 contact probe ($T_{max}$ < 600˚C) and a KA04 4 mm remote probe ($T_{max}$ < 750˚C). The left side of Figure 3 shows the same image in the visible. A high energy temperature gradient is observed with a measuring point with a contact temperature of 180˚C, a temperature measured at 4 mm of 96˚C and an ambient air temperature at 1 m of 25˚C.

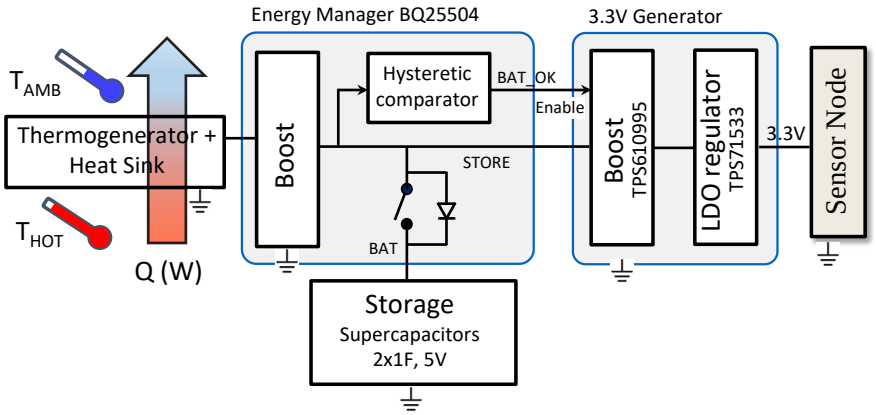


**Figure 1.** Overview of a power conversion chain.

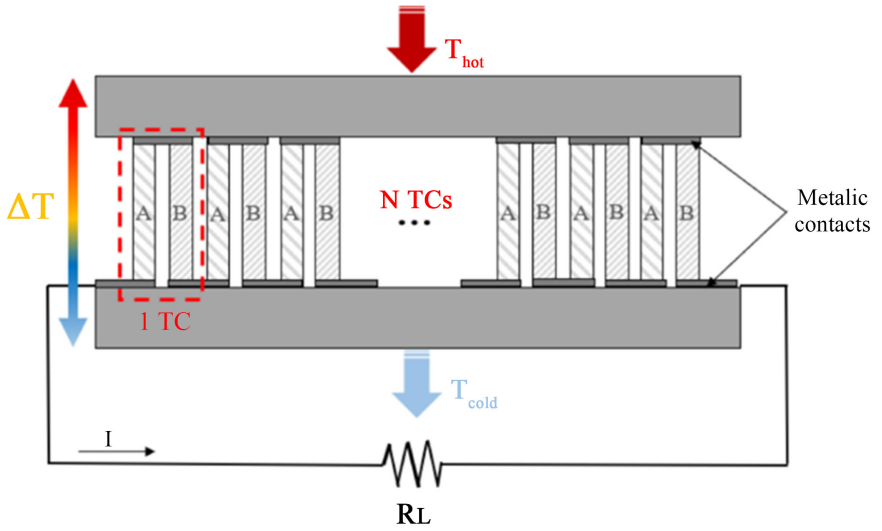


**Figure 2.** Basic principle of a typical thermoelectric generator.

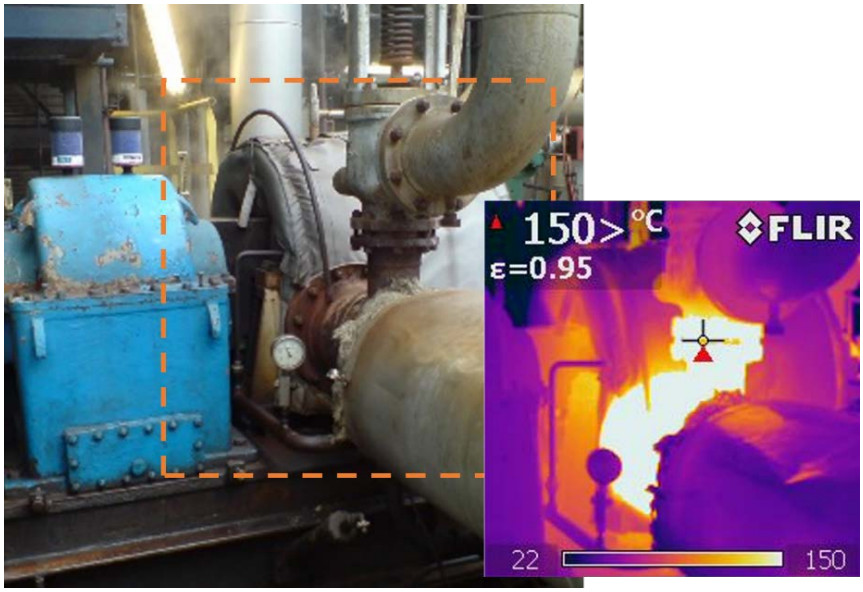


**Figure 3.** Visible and infrared photographs.

**Table 1.** Technical specifications of infrared camera.

| Parameters | |
|---|---|
| Temperature range | From −20˚C to 350˚C |
| Accuracy | ±2˚C |
| Image resolution | 180 × 180 pixels |
| Thermal sensitivity | <0.1˚C at 25˚C |
| Picture frequency | 9 Hz |

### 4.2. Modelisation of the TEG and It Heatsink

The main technical challenge of this study is to provide a thermal gradient across the TEG module sufficient for powering a sensor node while keeping the size of the energy harvesting module as small as possible. In our case, the chosen TEG and dissipator assembly is shown in **Figure 4**.

The TEG is electrically characterized by its Seebeck coefficient $\alpha$ ($V/^{\circ}C$) and its electrical resistance $R$ ($\Omega$). **Figure 5** presents the electrical and thermal modelling by the electrical analogy of the system, where the heat flux $Q$ ($W$), temperature $T$ ($^{\circ}C$) and thermal resistance $R_{th}$ ($^{\circ}C/W$) have as their respective analogues the current $I$ ($A$), the voltage $V$ ($V$) and the resistance $r$ ($\Omega$).

Using this, we obtain an electrical description of this model in (Equation (1)):

$$V_{TEG} = \alpha \cdot \Delta T_{TEG} - R \cdot I_{TEG} \tag{1}$$

The TEG and heatsink are modelled by their respective thermal resistances $R_{thTEG}$ and $R_{thHS}$ (*HS for heatsink*). To make the model easier to understand, two aluminium thicknesses have been omitted from **Figure 5**, one between the heatsink and the TEG and the other between the TEG and the heatsink. These can be included in the model by adding $R'_{th}$ and $R''_{th}$ in series, each of about 0.03 ˚C/W [30].

If we note $Q$ ($W$) the average heat flux through the TEG, $T_{HOT}$, $T_2$ and $T_{AMB}$ ($^{\circ}C$) the respective temperatures of the hot source, the TEG/sink interface, and the ambient air temperature, we obtain from the proposed model:

$$\Delta T = T_{HOT} - T_{AMB} = \left(R_{thTEG} + R_{thHS}\right) \cdot Q \tag{2}$$

And:

$$\Delta T_{TEG} = T_{HOT} - T_2 = R_{thTEG} \cdot Q \tag{3}$$

Therefore, the gradient $\Delta T_{TEG}$ across the TEG can be expressed by:

$$\Delta T_{TEG} = \frac{R_{thTEG}}{R_{thTEG} + R_{thHS}} \cdot \Delta T = \beta \cdot \Delta T \tag{4}$$

With:

$$\beta = \frac{R_{thTEG}}{R_{thTEG} + R_{thHS}} < 1 \tag{5}$$

This modelling assumes that the model parameters are constant, which is a valid assumption for small temperature variations [31]. It does not consider the

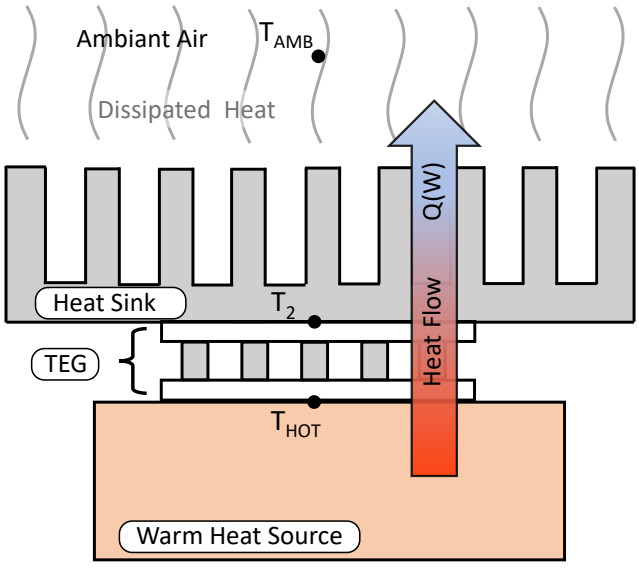


**Figure 4.** Simplified representation of a TEG inserted between its heatsink and a heat source.

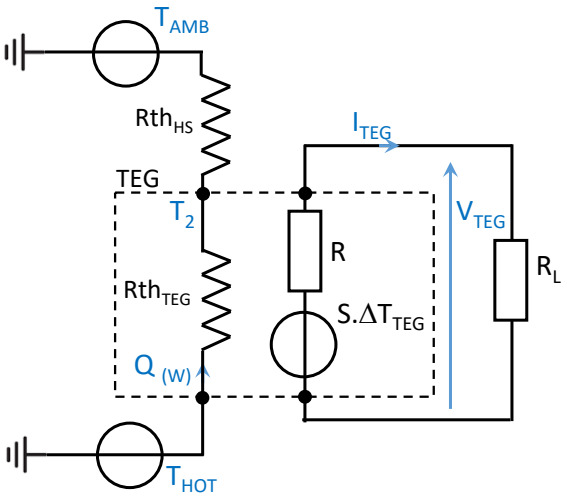


**Figure 5.** Electrical and thermal modelling by electrical analogy of the system.

dynamic aspects (*steady state is assumed*) or the more complex phenomena related to convection with the ambient air.

Nevertheless, it allows an estimate of the recoverable electrical power according to the TEG and the selected dissipator. In practice, we have found that the actual recovered power is 10% to 20% lower. This is due to the equivalent thermal resistance of the TEG $R_{thTEG}$. Assuming it is constant, it decreases as the TEG delivers current, reducing the gradient across the TEG and therefore the recoverable power [32]. In addition, uncertainties associated with heat exchange with the surroundings (*ventilated or not*, *variation of hotspot temperature*, *ambient air*, *etc.*) are important. It is therefore not useful to have a more refined model.

The open voltage $V_{OC}$ at the TEG terminals is defined by the following rela-

tionship:

$$V_{OC} = \alpha \cdot \Delta T_{TEG} \tag{6}$$

In general, the expression for the electrical power supplied by the TEG as a function of the TEG voltage is a parabola given by [33]:

$$P_{TEG} = \frac{1}{R} \cdot \left(V_{OC} - V_{TEG}\right) \cdot V_{TEG} \tag{7}$$

If the TEG flows on a adapted load $R_L$ ($R_L = R$), the electrical power is maximum and is:

$$P_{Max} = \frac{V_{OC}^2}{4R} = \frac{\left(\alpha \cdot \Delta T_{TEG}\right)^2}{4R} \tag{8}$$

The integrated circuit connected to the TEG will perform the electrical impedance matching by setting $V_{TEG}$ close to $\frac{V_{OC}}{2}$. In this case, maximising the electrical power means maximising $V_{OC}$ and therefore $\Delta T_{TEG}$. To do this, we will try to have the lowest possible thermal resistance ($\beta$ *close to* 1).

### 4.3. TEG and Its Dissipator Choices

The main criteria for selecting a TEG are temperature resistance, available surface area, performance (*Seebeck coefficient*, *electrical and thermal resistance*) and of course price [33].

In our application, as a high energy temperature gradient is observed with a measurement point with a contact temperature of 180˚C, we decided to choose an Eureca TEG1-30-30-8.5/200 [34]. In fact, this TEG can withstand 200˚C, which is suitable for the intended application. **Table 2** presents its specifications; **Figure 6** presents the TEG.

The TEG alone cannot guarantee the performance required for the overall system to function properly. It is essential to consider the TEG + heatsink assembly to obtain an optimized and efficient operation [35]:

- Heatsink should be chosen to favor the transfer of the heat flow with the ambient air and therefore with the lowest possible thermal resistance as expressed in the previous paragraph.

- The maximum exchange surface with the ambient air should therefore be achieved while maintaining acceptable dimensions and weight.

Therefore, a compromise had to be found. To ensure that, the device takes up as little space as possible and to avoid favoring one direction of airflow (*vertical or horizontal positioning*), we have chosen the Coolinnovations heatsink 3-202011M ($R_{thHS}$ = 4.7 *˚C/W in still air at atmospheric pressure*) [36]. If an air flow is present, or if the positioning of the device favors natural convection, the heat exchange is enhanced, and the thermal resistance of the heat sink is reduced ($R_{thHS}$ = 1.8 *˚C/W* @ 0.5 *m/s wind speed*). Conversely, if the air pressure drops (*such as in the case of a high-altitude aeronautical application*), the heat exchange between the heat sink and its environment slows down and the heat sink's thermal resistance increases.

**Table 2.** TEG1-30-30-8.5/200 specifications.

| | |
|---|---|
| Max. operation temperature | 200˚C |
| Thermal force | 0.054 V/K |
| Electric resistance | 3.4 Ω |
| Thermal conduction | 0.3 W/K |
| Size | 40 × 40 × 3.4 mm |
| Max. open circuit voltage | 10.8 V |
| Max. open circuit current | 7 A |
| Max. power | 19 W |

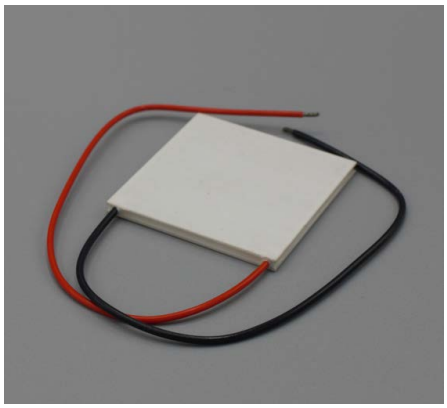

**Figure 6.** TEG1-30-30-8.5/200.

### 4.4. TEG and Heat Sink Assembly

To ensure thermal conduction, the whole system must be properly secured to the hot wall. For this purpose, a fixing with 8 Samarium Cobalt (*SmCo*) magnets ensures that the system is held in place even in the presence of vibrations [37]. The assembly ($60 \times 60 \times 40\ mm^3$) is shown in **Figures 7-9**.

The magnets ($T_{max} = 200\ ^{\circ}C$) are integrated into an aluminum part which conducts the heat to the TEG. The TEG is embedded in a hollow block of Teflon (*thermal insulation*), which is inserted between the aluminum support and the heat sink. Screws are used to secure the components together. Note that the positioning of the screws partially avoids thermal bridging between the hot wall and the heatsink (*Duration screws instead of stainless steel would have avoided thermal bridging*). The clamping pressure affects the power recovery [38], but this will not be investigated in this paper. A thin layer of high thermal conductivity grease (2.9 $W/m{\cdot}K$) is sandwiched between the elements to improve thermal contact. The quality of the thermal grease plays an important role, and it should be selected with the lowest thermal resistance.

In an industrial environment, the surface condition of machines is rarely perfect. It is therefore advisable to clean (*or even sand*) the target area before positioning the TEG. A thin layer of thermal grease will also be placed between the hot wall and the TEG base. The aim is to achieve the best possible thermal contact.

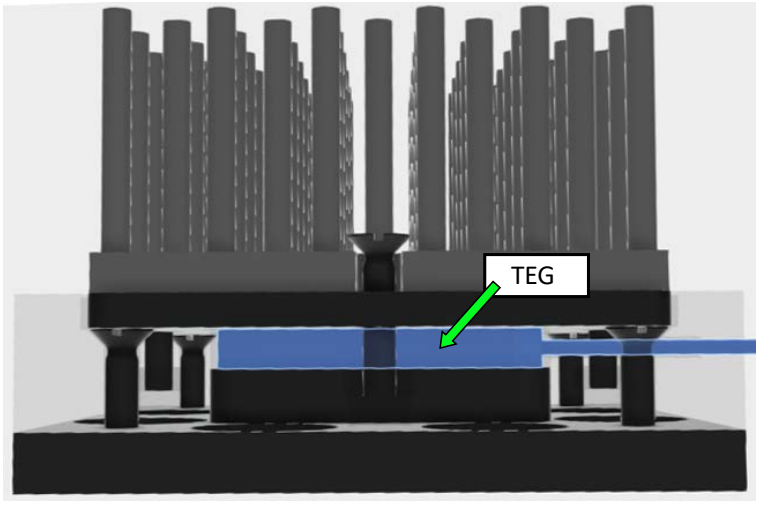


**Figure 7.** Exploded view of the device.

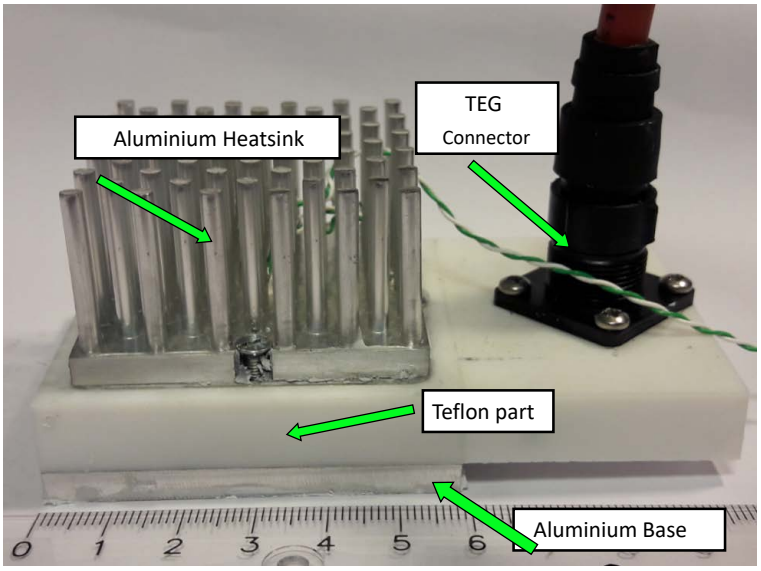


**Figure 8.** Assembled energy recovery unit.

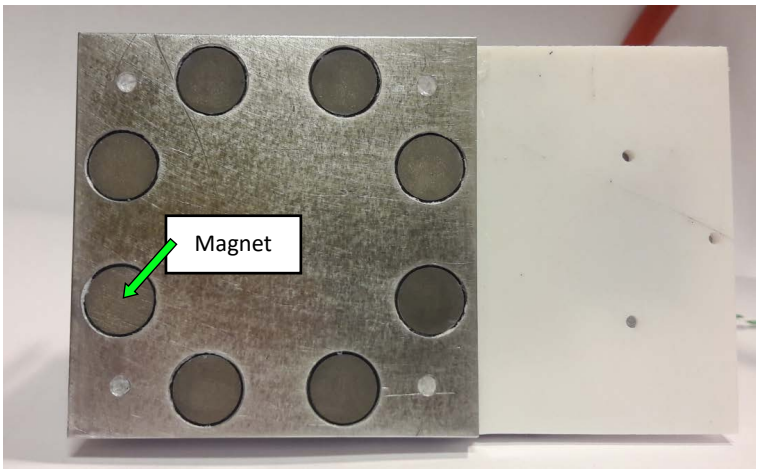


**Figure 9.** Bottom view with the 8 magnets.

## 4.5. Tests of the TEG + Dissipator Package

### 4.5.1. Test Bench Facility

To test the TEG and heatsink assembly, we use a magnetisable steel plate with temperature-controlled water flowing behind it.

Three thermocouples are used to measure $T_{HOT}$, $T_{AMB}$ and $T_2'$, where $T_2'$ is the temperature at the bottom of the heatsink. $T_2'$ is often confused with $T_2$ (*the temperature at the TEG/heatsink interface*). In fact, with a thickness of 5 mm for the plate between the TEG and the heatsink, 5 mm for the heatsink, an area $S$ of 3 × 3 cm$^2$ and a thermal conductivity $\lambda_{ALU}$ of 200 W/($m$·$K$), we find a thermal resistance $R_{th1}$ between the TEG/heatsink interface and the bottom of the heatsink given by the equation:

$$R_{th1} = \frac{L}{\lambda_{ALU} \cdot S} \tag{9}$$

Using this, $R_{th1}$ is evaluated around 0.05˚C/W. It would therefore take 20 W of heat flux to have only 1˚C difference between $T_2$ and $T_2'$, meaning $T_2$ and $T_2'$ are very closed (cf *Equation* (2))

### 4.5.2. Transient Analysis

The TEG and heatsink assembly, initially at room temperature, is attached to the hot plate using magnets (*a thin layer of thermal grease is first applied to the bottom of the energy recovery unit*). The evolution of the open circuit voltage $V_{OC}$ and temperature $T_2'$ are then recorded (**Figure 10**).

$V_{OC}$ increases rapidly to reach 1.35 V and then falls back to stabilize at 0.5 V once steady state is reached. This is a comprehensive behavior as the initial available gradient decreases as the heat sink temperature increases.

This test highlights the dynamics of the system (*which can be modelled for $T_2$ and $V_{OC}$ by a first order time constant $\tau$ = 3.5 min*). It also shows us that we should not confuse $\Delta T$ and $\Delta T_{TEG}$. With the assumption $T_2' \approx T_2$, the calculation of the ratio $\frac{\Delta T_{TEG}}{V_{OC\_TEG}}$ gives $\alpha$ = 30 mV/˚C. This value of $\alpha$ is much lower than

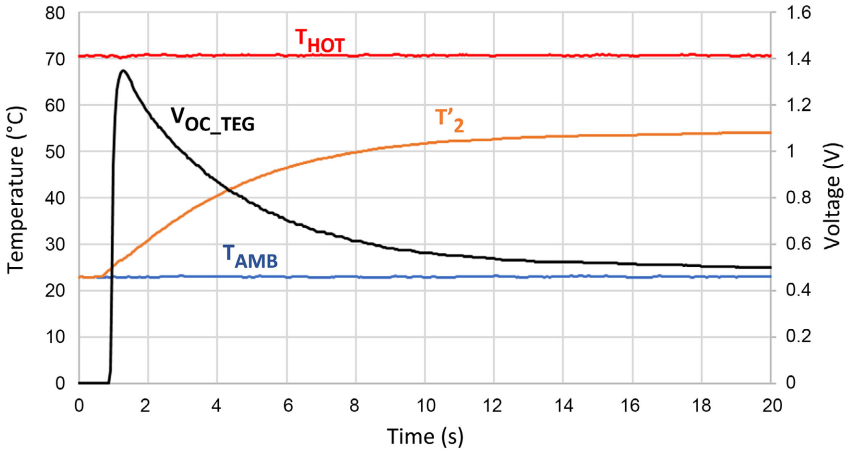


**Figure 10.** Evolution of open voltage $V_{OC}$ and temperature $T_2'$.

the value given in the technical documentation (53 $mV/^{\circ}C$), but it has been verified experimentally with another experiment, in which a hot source was applied to one side of the TEG and a cold source to the other. It is possible that this TEG was partially deteriorated in tests prior to the present study.

$\beta = \frac{\Delta T_{TEG}}{\Delta T}$ is 0.35, which makes it possible to find $R_{thHS}$ knowing $R_{thTEG}$.

The calculation gives $R_{thHS}$ = 6˚C/W. This value is consistent with the manufacturer's data (4.7 $^{\circ}C/W$). The supplier's characterization of the heatsink generally uses a heat source with a surface area equal to that of the heatsink, but in the case studied, the surface area of the TEG is smaller than that of the heatsink, which impedes heat transfer and therefore increases the thermal resistance.

#### 4.5.3. Evolution of Pmax vs ITEG

Once steady state has been reached, the open circuit voltage is recorded as $V_{OC,ITEG=0}$. **Figure 11** presents *I(V)* and *P(V)* characteristics with $\Delta T$ constant, ($T_{HOT}$ = 70 $^{\circ}C$, $T_{AMB}$ = 23 $^{\circ}C$) but two different initial operating points.

With an active load or by varying the resistance of a potentiometer, the operating point is varied (*curves A in* **Figure 11**, *taken from* $V_{OC,ITEG=0}$). The active load then maintains $V_{TEG}$ such that $V_{TEG} = \frac{V_{OC\_ITEG=0}}{2}$.

Once the new steady state is reached (*around* 20 *min.*), and after the $I_{TEG}$ current has stabilised, the new characteristics *P(V)* and *I(V)* for $V_{TEG} = \frac{V_{OC\_ITEG=0}}{2}$ are plotted "quickly" (*with respect to the dynamics of the system*) (*B curves*).

A decrease in maximum power of the order of 10% is observed. The reason for this decrease was briefly described at the end of section 3.2. This also shows us that the characteristic measured after the open-circuit steady state leads to an overestimation of the recoverable power by about 10% compared to the steady state operation at $P_{max}$. The slope of the *I(V)* curves allows us to estimate the serial resistance *R*. A value of around 5 Ω is found, which is slightly higher than the value predicted by the manufacturer's data (3.4 $\Omega$) but is still consistent.

## 5. Energy Harvesting Circuits

Various commercially available integrated circuits can extract energy from solar cells or TEGs, such as BQ25504 [39], BQ25570 [40], both available as demo board, or SPV1050 [41], MAX17710 [42] or ADP5090 [43]. These ICs support both Maximum Power Point Tracking (*MPPT*) functionality and the charging of a storage element (*rechargeable battery or supercapacitor*).

### 5.1. BQ25504 Study

Given the relatively low levels of $V_{TEG}$ voltage levels expected, we chose to use the BQ25504 from Texas Instrument for this project. **Table 3** presents its main characteristics.

This circuit is designed to recharge and manage a battery (*which explains the*

*$V_{BAT}$ notation in the technical documentation*) or supercapacitors. We will use it in the latter configuration (Figure 12).

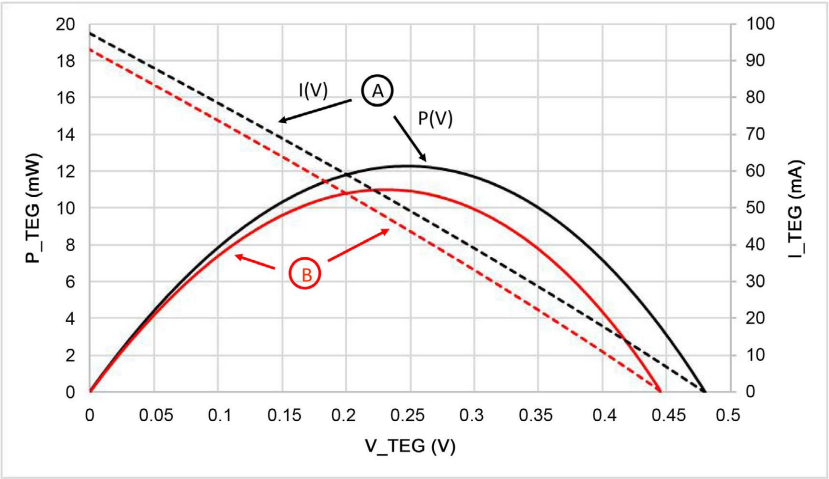


Figure 11. $I(V)$ and $P(V)$ characteristics with $\Delta T$ constant, ($T_{HOT}$ = 70˚C, $T_{AMB}$ = 23˚C) but two different initial operating points.

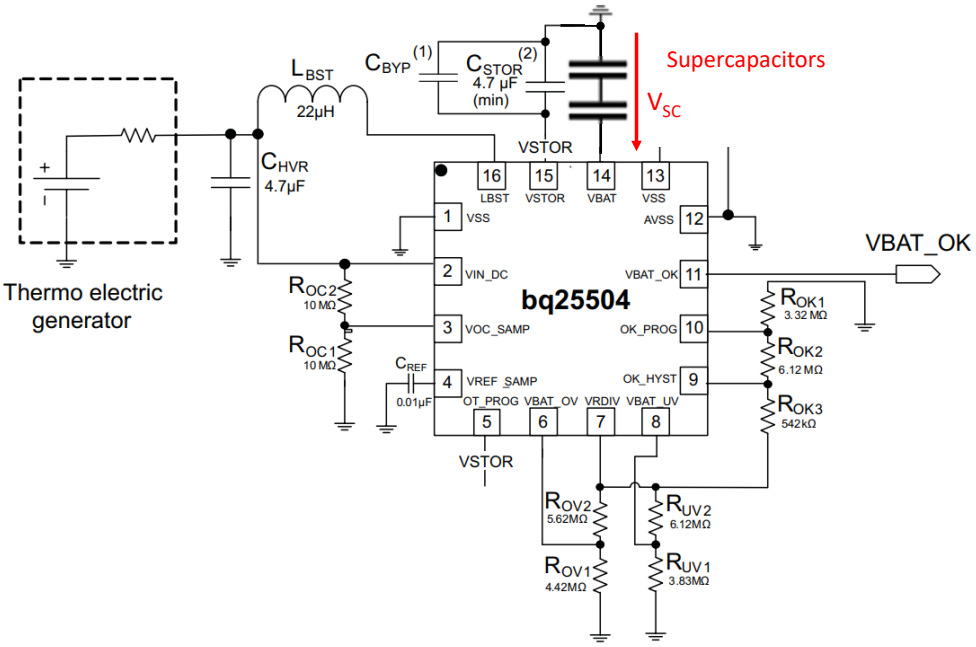


Figure 12. BQ25504 associated to a TEG and supercapacitors.

Table 3. BQ25504 characteristic.

| | |
|---|---|
| Input voltage on the thermos-generator side ($V_{IN}$) | between 0.13 and 3.0 V |
| Minimum start-up voltage | 0.6 V |
| Input current ($I_{IN}$) | limited to 100 mA |
| Storage stage voltage ($V_{SC}$) | <5.25 V |
| Circuit consumption in standby mode | <1 µA |
| Maximal temperature | 80˚C with OT_PTOG connected on V_STORE |

### 5.1.1. Disconnect Transistor

Figure 13 shows an internal transistor in the BQ25504 that allows the disconnection of the storage stage when the voltage of the storage stage is too low.

Its behavior can be described as follows:

- Before the first start-up, this transistor is open.

- It closes when the $V_{STOR}$ voltage reaches 2.3 V and remains closed unless $V_{STOR}$ falls below this threshold with a hysteresis effect.

- Once the transistor is closed, $V_{STOR} = V_{SC}$.

- $V_{STOR}$ is then the voltage across the supercapacitors.

When the transistor is open, the supercapacitors can no longer discharge. Note the diode in parallel with this transistor, which allows the supercapacitors to charge regardless of the state of the transistor.

### 5.1.2. Boost + MPPT

A boost DC/DC converter is placed between the TEG and the storage stage.

If the $V_{STOR}$ voltage has not reached a minimum threshold of around 1.8 V, the boost operates in a degraded mode with a poor conversion efficiency (*between* 10% *and* 50%). When the threshold is reached, the boost switches to normal operation.

For $V_{STOR}$ between 1.8 V and $V_{BAT\_OV}$ = 4.9 V, the converter operates in Maximum Power Tracking Mode (*MPPT mode*) with a so-called fraction of $V_{OC}$ algorithm.

Every 16 s and for 256 ms, the TEG is disconnected, allowing the BQ25504 to measure the open circuit voltage ( $V_{OC}$). After that, the DC/DC operates by regulating the TEG voltage to a setpoint voltage equal to $V_{MPP} = \frac{V_{OC}}{2}$.

However, if the storage stage is full, *i.e.*, when $V_{STOR}$ reaches $V_{BAT\_OV}$, and as long as:

$$V_{STOR} < V_{EOC} - 50\text{ mV}$$

DC/DC converter shuts down to avoid overload. Also note the active limitation of the BQ25504 circuit to 100 mA on the input current.

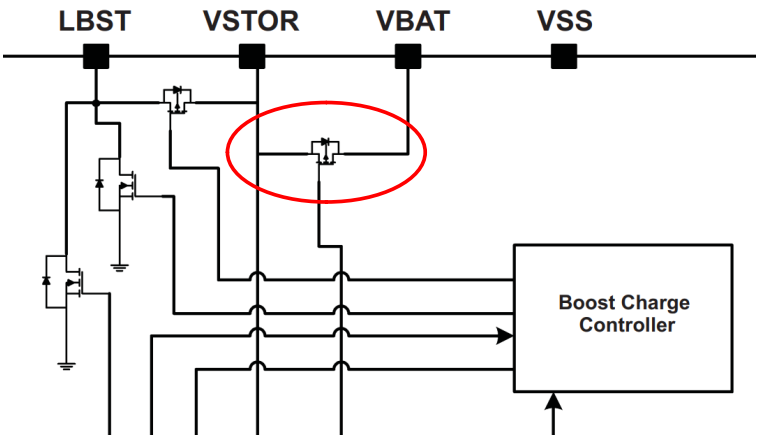


**Figure 13.** Internal transistor in the BQ25504.

### 5.1.3. Internal Comparator

$V_{BAT\_OK}$ output activates the boost converter located at the input of the block which generates and regulates the 3.3 V. The voltage measured by the comparator is the $V_{STOR}$ voltage. $V_{STOR}$ is equal to $V_{SC}$ as soon as the internal switch is ON. By the following, we note $V_{BAT\_H}$ and $V_{BAT\_L}$ the high and low thresholds of the comparator. To ensure a fast initial start, we took $V_{BAT\_H}$ = 3 V; $V_{BAT\_L}$ is fixed at the minimum level, *i.e.*, 2.3 V.

## 5.2. Test

For this test, the TEG is placed on a hot plate with thermal paste in between. Temperature measurements are taken with thermocouples and give $T_{HOT}$ = 170˚C and $T_{AMB}$ = 25˚C. Electrical measurements are made using a power meter (*N*6705*B*). No load is connected to the supercapacitors. Note that the charging is fast (180 s) because the gradient is high (Figure 14).

Planned phases can be well observed:

- **Phase 1**: In this "COLD START phase", $V_{STOR}$ goes from 0 V to 1.8 V. As soon as $V_{STOR}$ reaches 1.8 V, the next phase begins.

- **Phase 2:** boost converter is operational in MPPT mode. The current from the TEG increases significantly to 55 mA. The TEG voltage is close to $\frac{V_{OC}}{2}$, *i.e.*, 1.05 V. The internal transistor between $V_{BAT}$ and $V_{STOR}$ is open, but the supercapacitors are charged by the current flowing through the internal diode of this transistor. The difference between the voltages $V_{STOR}$ and $V_{SC}$ corresponds to the potential seen by this diode. When $V_{STOR}$ is close to 2.2 V, the transistor closes and opens (*driving around* 2.2 *V on* $V_{STOR}$ *with a hysteresis effect*).

- **Phase 3:** As soon as $V_{STOR}$ is above 2.2 V, the internal transistor remains closed, and the supercapacitors continue to charge. Until $V_{BAT\_OV}$, boost is in MPPT mode. The TEG open-circuit phases are repeated every 16 s; the $I_{TEG}$ current drops to zero and the TEG voltage (*not visible on this graph due to the low sampling rate of the apparatus*) briefly rises to 2.1 V.

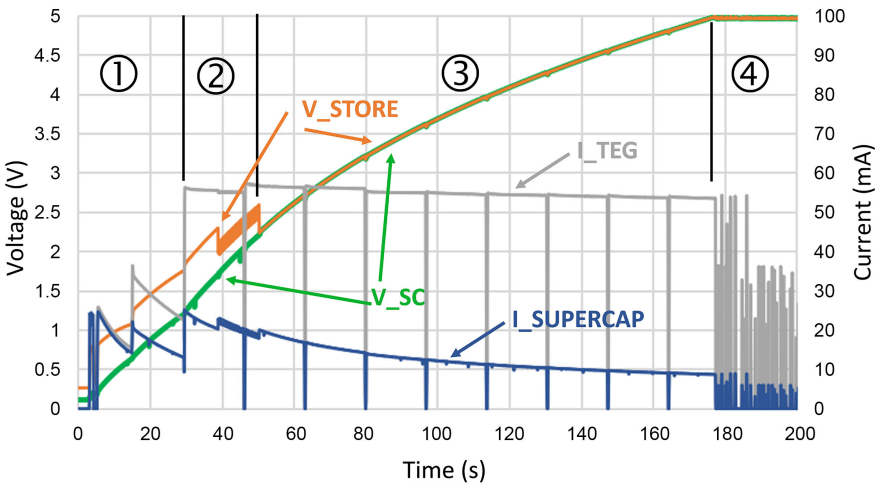


Figure 14. Voltage and current characteristics.

- **Phase 4:** $V_{STOR}$ is near $V_{BAT\_OV}$. The supercapacitors are fully charged. The boost circuit of the BQ25504 works intermittently to compensate the losses (*hysteresis around* $V_{BAT\_OV}$).

### 5.3. BQ25504 Efficiency

Several tests were carried out with different hot-side temperatures and therefore different $V_{TEG}$ voltages. The efficiency remains above 80% if $V_{TEG} > 0.4$ V, $V_{SC} > 2.2$ V and $I_{TEG} > 0.1$ mA (**Figure 15**). On the other hand, the efficiency decreases sharply at low $V_{SC}$ voltages. It is therefore advisable to avoid discharging the supercapacitors below 2.2 V, so that only the initial start-up phase is carried out at low efficiency.

## 6. Storage Stage

The choice of supercapacitors is always in competition with the choice of a rechargeable battery [44]. For our application, which presents a quasi-permanent temperature gradient, supercapacitors are interesting for their temperature resistance and, to a lesser extent, for their cycling resistance (*in the case of loads with consuming phases that partially empty the supercapacitors*). For our application, we choose a PowerStor supercapacitor, with the characteristics shown in **Table 4** [45].

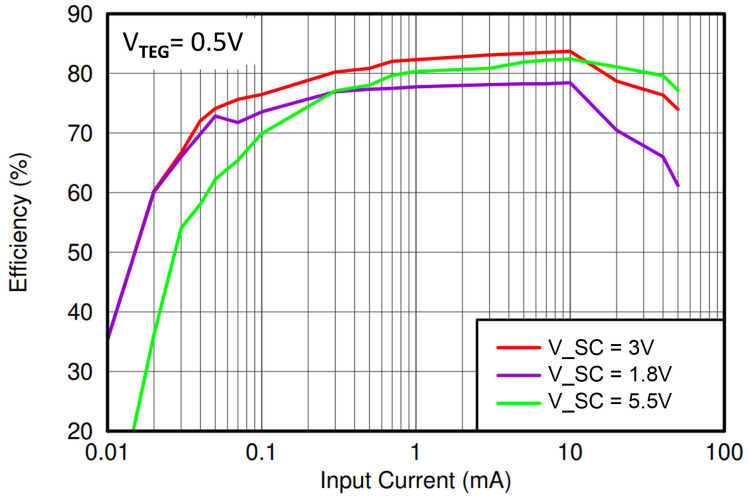


**Figure 15.** Example of BQ25504 efficiency [39].

**Table 4.** Powerstor-B0810-2R5105-R characteristics [45].

| Capacitance $C$ | 1 F |
|---|---|
| Voltage | 2.5 V |
| Leakage current | 4 μA |
| ESR series resistance | 0.5 Ω |
| Maximal temperature | 80˚C |

### 6.1. Sizing

For this project we choose to store the energy under a maximum voltage $V_{BAT\_OV}$ = 4.9 V, corresponding to the association of two supercapacitors in series.

The maximum charge level remains below the maximum achievable, which is 5.0 V for the supercapacitors, 5.25 V for the BQ25504 and 5.5 V for the TPS610995 [46]. This ensures a safe range for the system.

If we note $C_{EQ}$ The equivalent capacitance of the two supercapacitors in series, this is done by:

$$C_{EQ} = \frac{C_{EQ}}{2} = 0.5\ \text{F} \tag{10}$$

The energy of the pack is given by the relation:

$$E_{SC} = \frac{1}{2} \cdot C_{EQ} \cdot V_{SC}^2 \tag{11}$$

We note $\eta_{3.3}$ the average efficiency of the stage that provides the 3.3 V, taken to be 0.7.

#### 6.1.1. Start-Up Criterion

The output stage is activated for $V_{SC} = V_{STORE} = V_{BAT\_H}$ with $V_{BAT\_H}$ chosen to be 3 V. When the sensor is started, the voltage across the supercapacitors decreases. It must remain at a sufficient level for the correct operation of the output boost (*above* 0.7 *V*).

At the end of the start-up, $V_{SC} = V_{STORE} > V_{BAT\_L}$. $V_{BAT\_L}$ is chosen at 2.3 V. With the chosen value of *C*, the following relationship is validated:

$$E_{SC(VSC=VBAT_H)} \geq E_{SC(VSC=VBAT_L)} + \frac{E_{STARTUP}}{\eta_{3.3}} \tag{12}$$

#### 6.1.2. Autonomy Criterion

Once the supercapacitors are charged, the system should have 1 hour of autonomy, this value is sufficient because the gradient is permanent. *N* is the number of cycles that can be performed in 1 hour ($T_{CYCLE}$ = 25.8 *s,* $N$ = 140). The self-discharge of the supercapacitors is neglected. The maximum charge level of the supercapacitors is $V_{BAT\_OV}$ and the minimum level is $V_{BAT\_L}$. We check that the following relationship is valid with the chosen values:

$$E_{SC(VSC=VBAT\_0V)} - E_{SC(VSC=VBA\_L)} \geq \frac{N \cdot E_{CYCLE}}{\eta_{3.3}} \tag{13}$$

### 6.2. Self-Discharge

Since energy recovery is normally always active, self-discharge is not very important for the case under consideration (*provided the recovered energy is sufficient*).

### 6.3. Balancing Circuit

For "small" supercapacitors (<10 *F per cell*), experience has shown that a balancing circuit is not necessary if the supercapacitors have the same initial capa-

citance value and remain at the same temperature, which is the case for this application.

As the self-discharge current varies with the voltage, a natural balancing occurs.

## 7. 3.3 V Generation

Several solutions have been considered using the supercapacitor stage to deliver 3.3 V to the load:

- First uses a boost converter. But this limits the supercapacitor voltage to 3.3 V.

- The second uses an LDO. But the supercapacitors must be kept above 3.3 V.

- The third solution uses a buck/boost (TPS63001) and can be as efficient as the solution shown below.

The chosen solution cascades a boost (*TPS*610995) [46] and an LDO (*TPS*71533) [47]. This solution combines the use of supercapacitors over a wide range from 2.3 V to 4.9 V (75% *of the stored energy at a maximum level of* 5 *V is usable*) with an efficiency of more than 80% at $V_{SC} < 3.6$ V.

The TPS610995 is enabled (*pin Enable*) by the $V_{BAT_}$OK logic signal from the BQ25504 as soon as the supercapacitor voltage is sufficient. It can deliver up to 800mA over a voltage range of 0.7 to 5.5 V. It has standby currents minor to 1 µA when disabled (*Enable at Low level*). It provides 3.6 V output when the input voltage is below 3.65 V. Beyond that, the regulation is inoperative and the boost delivers the input voltage at the output, except for the voltage drop across the internal diode, which is negligible.

The TPS71533 LDO delivers 3.3 V at the output. It accepts an input voltage between 2.5 V and 24 V and delivers a maximum current of 60 mA. Its current consumption remains low (<3.2 $\mu A$). It operates with very good efficiency as long as $V_{SC} < 3.65$ V; beyond that, the voltage drop at its terminals increases, which reduces its performance.

To increase the output current beyond 60 mA, this component should be replaced.

## 8. Tests and Results

### 8.1. Test Solution

To test the developed energy harvesting solutions, we used a communicating sensor node based on a Jennic 5148 module. This module accepts a $V_{JEN}$ supply voltage between 2.4 and 3.6 V. The communication protocol is Zigbee, and the system has a maximum range between the sensor node and the coordinator of about 20 m. The radio information is retrieved by the coordinator module of the sensor network, then redirected via a wired serial link to a PC.

### 8.2. Power Consumption

Using a 3.3 V regulated power supply, we measured the current supplied to the

module to calculate its consumption (*measured with an Agilent DC power analyser N6705B*) [48].

**Initialization.**

Once the sensor node is connected to the network, the power consumption is substantial. The energy $E_{STARTUP}$ required to start is measured at 0.35 J after 20 s. The current during start-up is shown in Figure 16.

**After initialization.**

Once the initialization phase is over, the operating cycle is divided into two phases:

- An active phase during which the measurements, their processing and the radio transmission are carried out.

- A standby phase with very low consumption. The standby phase is periodically interspersed with very short radio transmissions ("*beacon*") to remind the user that the module is present on the network.

These phases can be seen in the chronogram in Figure 17.

The analysis of the consumption gives the following results: one measurement cycles every 25.8 s (*measurement duration* 112 *ms*, *consumption* 22 *mA*), between 2 measurements: 7 beacons (*one beacon every* 3.22 *s*, *duration* 8 *ms at* 21 *mA*), the rest of the time, the system is in sleep mode (*sleep mode* 4.3 *μA*) This gives a consumption per cycle $E_{CYCLE}$ = 12.4 mJ, and an average power $P_{CYCLE} \approx 0.5$ mW .

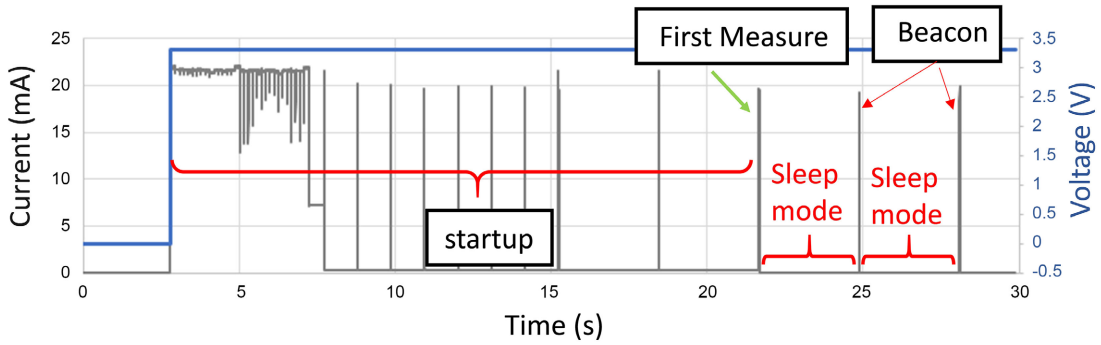


Figure 16. Initial start-up of the module.

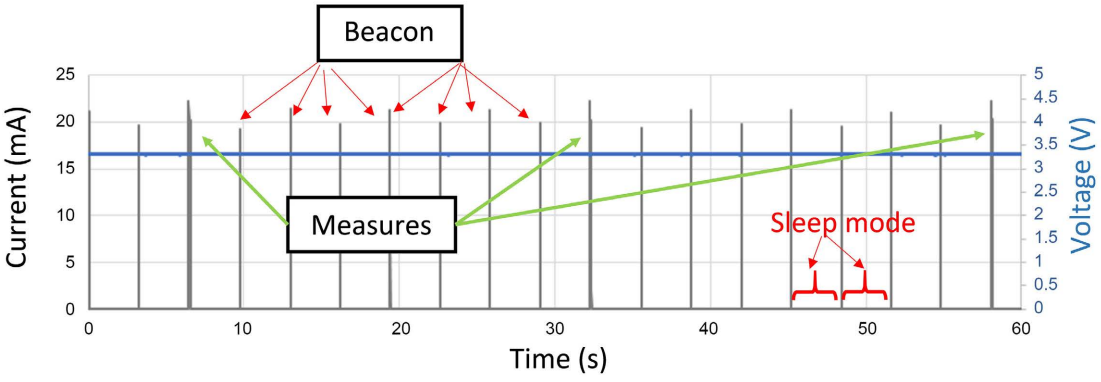


Figure 17. Operating voltage and current.

### 8.3. Final Circuit

Figure 18 shows the electrical diagram of the whole device. The electronics are integrated on the board shown in Figure 19. The size of the board is 4 × 5 cm$^2$.

Between each stage of the board, a 0 Ω resistor is imprinted. These resistors are first not soldered on, so that the stages can be tested separately, and then the resistors are added, connecting the stages together. Test points are placed on the presented prototype but are not present on the final version.

The whole system is placed in a box connected to the TEG by a high temperature resistant silicon insulated cable. The price of the complete system is close to 60€ for the whole board (*for a set of* 250, *including* 17€ *for the TEG and* 2€ *for the magnets*).

At the beginning of the test shown in Figure 20, the TEG has been fixed on the hot surface for 30 minutes, where we can measure $T_{HOT}$ = 75˚C and $T_{AMB}$ = 23˚C. The supercapacitors are short-circuited.

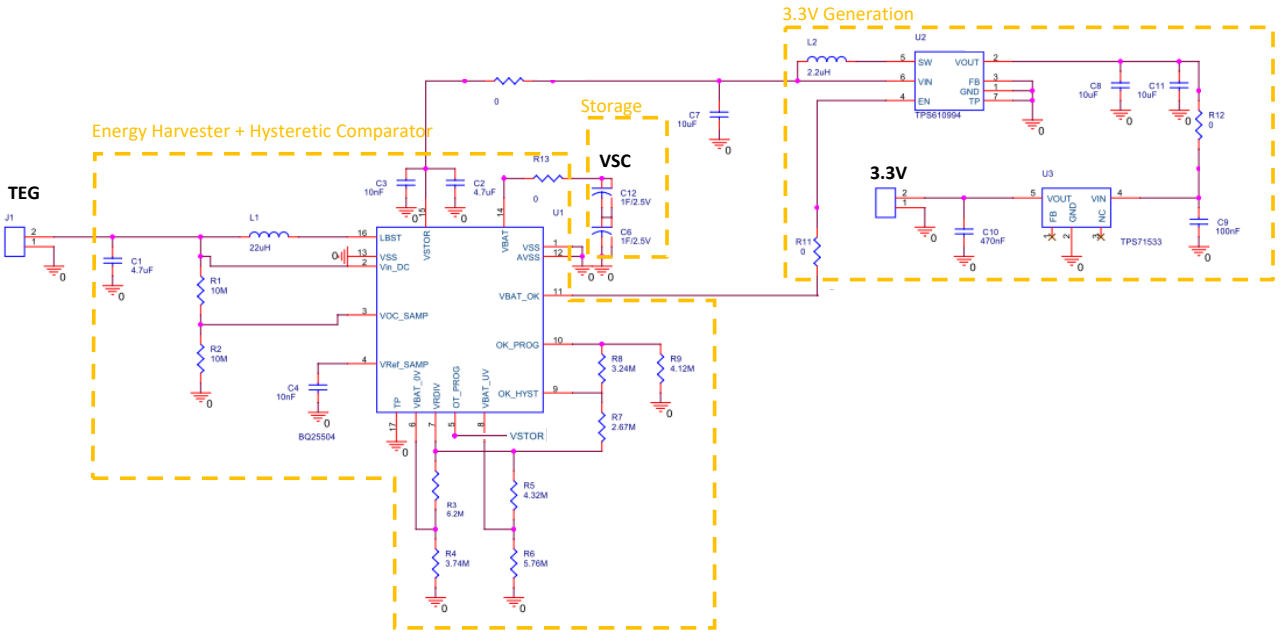


Figure 18. Electrical diagram of the whole device.


Figure 19. Electronic board.

- At $t = 0$ s, the short circuit is removed; the BQ25504 is in the cold start phase, the recovered power is low.

- As soon as $V_{SC}$ reaches 1.5 V, the circuit switches to MPPT mode ($V_{TEG} \approx \frac{V_{OC}}{2}$) and maximises the recovered power (5 *mW at the supercapacitors*).

- At $V_{SC} = 3$ V, the output voltage is switched on to 3.3 V, the sensor module is powered and starts up, which causes a sharp drop in $V_{SC}$.

- When the supercapacitors are charged, the recovered power decreases and just compensates the consumption of the sensor module.

Figure 21 shows the autonomy of the system.

- At $t = t_1$, the TEG is removed from the hot plate. It thermalises rapidly and the $V_{TEG}$ drops. The measured autonomy is 2 h 50 mn, which is higher than the initial estimate of 2 h obtained for an efficiency $\eta_{3.3}$ of 0.7. This means that the average efficiency of the assembly that generates the 3.3 V is higher than 0.8 (We also found that the consumption of the Jennic module decreases after a certain time of operation).

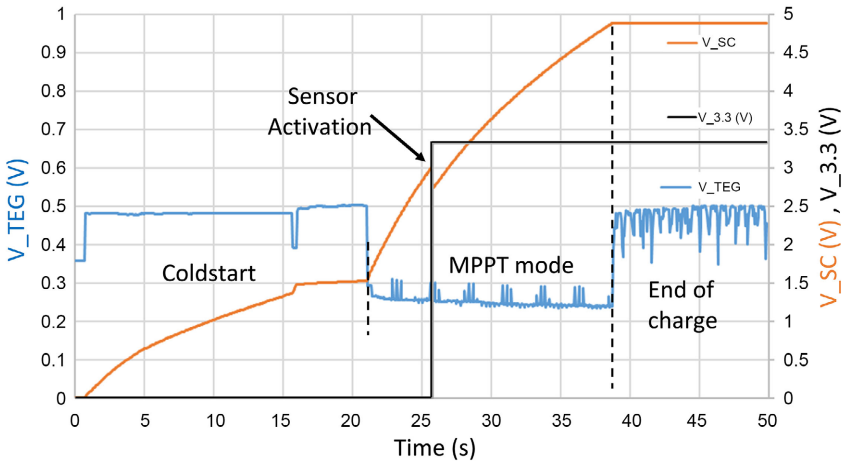


Figure 20. Start with $T_{HOT}$ = 75˚C and $T_{AMB}$ = 23˚C.

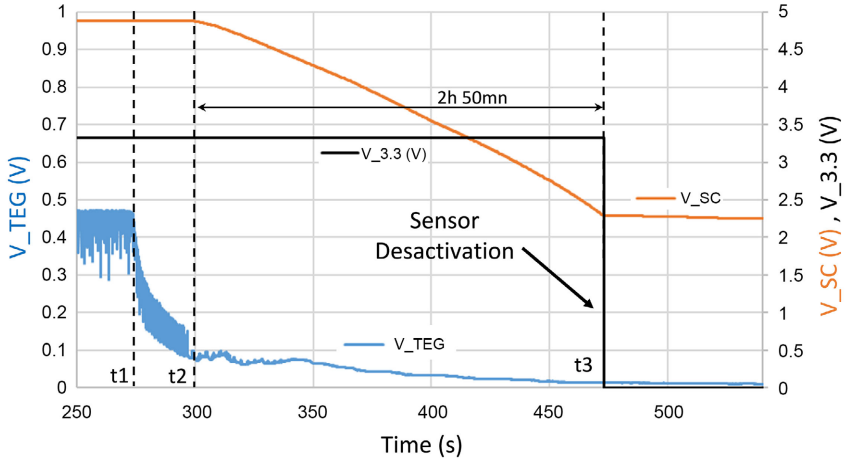


Figure 21. Stand-alone operation mode.

- At $t = t_3$, the stage that generates the 3.3 V is disconnected, the supercapacitors then empty very slowly (*supercapacitor self-discharge* + *low parasitic consumption around the BQ*25504 *and TPS*610995).

## 9. Discussion

Analysis of the results over several weeks shows that the presence of a permanent thermal gradient does not lead to service interruption: the measurements are then permanent, and the size of the storage element could have been reduced.

In the case of an intermittent thermal gradient, several strategies can be adopted, particularly in the case of non-critical data acquisition:

1) The loss of data is not critical: the chosen rate of measurement allows a representative average to be taken of the system's operation.

2) The data varies little over time and the increase in time between two measurements is acceptable. On the same principle, a detection of a significant variation in the measurement can order to start the acquisition system.

3) A more refined data acquisition strategy can be applied, in which the state of charge of the storage element dictates the rate of measurement and transmission, as well as the management of standby times.

It should also be noted that the measurements were carried out on a system in which a strong temperature gradient was present, resulting in sufficient recovered energy to ensure the desired and high measurement rate. This clearly shows the importance of measuring the temperature gradient in the system in order to assess the range of recoverable energy [49].

## 10. Conclusion

This paper presents the realization of an autonomous power supply (3.3 *V*, 60 *mA*) using the energy provided by a thermal gradient present between the two sides of a thermo-generator.

The system consists of two parts:

- The first part, consisting of a thermogenerator associated with a heat sink, can be used for temperatures up to 200˚C. Magnetic attachment makes it easy to use on flat metal surfaces.

- The second part is an electronic board that extracts, stores, shapes and manages the stored energy and can be placed close to the sensor. Note that this electronic board can operate at temperatures of up to 80˚C.

- The two parts are separated and connected by a high temperature cable, allowing the electronics to be moved to a less hot area. Storage is provided by supercapacitors.

In an industrial environment, close to permanent sources of heat, this type of power supply should allow perpetual operation. Compared to a battery solution, there is an initial cost premium. However, in the long term, the absence of maintenance (*battery replacement*, *cost of personnel dedicated to changing the batteries*, *etc.*) puts the two options in competition. Depending on the duration of use

and the authorised volume, the TEG solution may be more advantageous.

In addition, we found that the experimental conditions (surface condition of the hot source, horizontal or vertical position of the TEG, and sealing between the parts, etc.) have a significant influence on the performance of the TEG and heat sink assembly. Finally, it is worth noting that it is worth moving the heat sink further away from the hot source to increase the available gradient and therefore the recoverable electrical power. Similarly, while volume is not a constraint, a large heatsink with a large surface area for exchange with the air means that the system operates more optimally.

## Acknowledgements

This work was carried out as part of the 2ido project (*Internet Industriel Des Objets et Des Opérateurs*) financed by the BPI (*Banque Public d'Investissement*) as part of a PIA (*Programme d'Investissements d'Avenir*). The authors thank Xavier Dollat from LAAS-CNRS for the mechanical study and realisation.

## Conflicts of Interest

The authors declare no conflicts of interest regarding the publication of this paper.

## References

[1] (2018) Programme d'investissements d'avenir, Grands défis du numérique. https://www.entreprises.gouv.fr/files/files/directions_services/numerique/appels-a-projets/dp-defis-numerique-5vagues.pdf

[2] Omer, A., Khairi, I., Chia Ai, O. and Kamran Liaquat, B. (2022) Battery Characterization for Wireless Sensor Network Applications to Investigate the Effect of Load on Surface Temperatures. *Royal Society Open Science*, **9**, Article 210870. https://doi.org/10.1098/rsos.210870

[3] Hidalgo-Leon, R., Urquizo, J., Silva, C.E., Silva-Leon, J., Wu, J., Singh, P. and Soriano, G. (2022) Powering Nodes of Wireless Sensor Networks with Energy Harvesters for Intelligent Buildings: A Review. *Energy Reports*, **8**, 3809-3826. https://doi.org/10.1016/j.egyr.2022.02.280

[4] Boitier, V., Estibals, B., Huet, F. and Seguier, L. (2023) Battery-Free Power Supply for Wireless Sensor Combining Photovoltaic Cells and Supercapacitors. *Energy and Power Engineering*, **15**, 151-179. https://doi.org/10.4236/epe.2023.153007

[5] Champier, D. (2017) Thermoélectric Generators: A Review of Applications. *Energy Conversion and Management*, **140**, 167-181. https://doi.org/10.1016/j.enconman.2017.02.070

[6] Jaziri, N., Gutzeit, N., Bartsch, H., Boughamoura, A., Müllera, J. and Tounsi, F. (2022) LTCC-Based Y-Type Thermoelectric Generator with an Improved Heat Flow Guide for Automotive Waste Heat Recovery. *Sustainable Energy Fuels*, **6**, 2330-2342. https://doi.org/10.1039/D2SE00048B

[7] Fan, W., An, Z., Liu, F., Gao, Z., Zhang, M., Fu, C., Zhu, T., Liu, Q. and Zhao, X. (2023) High-Performance Stretchable Thermoelectric Generator for Self-Powered Wearable Electronics. *Advanced Science*, **10**, Article ID: 2206397. https://doi.org/10.1002/advs.202206397

[8] Álvarez-Carulla, A., Saiz-Vela, A., Puig-Vidal, M., *et al.* (2023) High-Efficient Energy Harvesting Architecture for Self-Powered Thermal-Monitoring Wireless Sensor Node Based on a Single Thermoelectric Generator. *Scientific Reports*, **13**, Article No. 1637. https://doi.org/10.1038/s41598-023-28378-6

[9] Zhu, S., Miao, L., Peng, Y., Gao, J., Lai, H., Liu, C., Zhang, Y., Zhang, X., Chen, Z. and Pei, Y. (2023) Persistently Self-Powered Wearable Thermoelectric Generator Enabled by Phase-Change Inorganics as the Heat Sink. *Materials Today Physics*, **32**, Article ID: 101011. https://doi.org/10.1016/j.mtphys.2023.101011

[10] Liu, Z., Cheng, K., Wang, Z., Wang, Y., Ha, C. and Qin, J. (2023) Performance Analysis of the Heat Pipe-Based Thermoelectric Generator (HP-TEG) Energy System Using *in-situ* Resource for Heat Storage Applied to the Early-Period Lunar Base. *Applied Thermal Engineering*, **218**, Article ID: 119303. https://doi.org/10.1016/j.applthermaleng.2022.119303

[11] Jaziri, N., Boughamoura, A., Müller, J., *et al.* (2019) A Comprehensive Review of Thermoelectric Generators: Technologies and Common Applications. *Energy Reports*, **6**, 264-287. https://doi.org/10.1016/j.egyr.2019.12.011

[12] Shen, Z.G., Tian, L.L. and Liu, X. (2019) Automotive Exhaust Thermoelectric Generators: Current Status, Challenges and Future Prospects. *Energy Conversion and Management*, **195**, 1138-1173. https://doi.org/10.1016/j.enconman.2019.05.087

[13] Zoui, M.A., Bentouba, S., Stocholm, J.G. and Bourouis, M. (2020) A Review on Thermoelectric Generators: Progress and Applications. *Energies*, **13**, Article 3606. https://doi.org/10.3390/en13143606

[14] Park, H. and Lee, D. (2019) Energy Harvesting Using Thermoelectricity for IoT (Internet of Things) and E-Skin Sensors. *Journal of Physics*: *Energy*, **1**, Article ID: 042001. https://doi.org/10.1088/2515-7655/ab2f1e

[15] (2023) Wireless Industry Sensors Free from Battery Dependency. https://dcosystems.co.uk/wireless-industry-sensors/

[16] (2023) Autonomous Sensors for the Industry. https://moiz-eh.com/

[17] (2023) Biolite. https://www.bioliteenergy.com/collections/portable-stoves

[18] (2023) TEG10W Stove Top TEG Generator. https://thermoelectric-generator.com/product/teg10w-stove-top-teg-generator/

[19] Mathis, S., Gruber, J.M., Ebi, C., Bloem, S., Rieckermann, J. and Blumensaat, F. (2022) Energy Self-Sufficient Systems for Monitoring Sewer Networks. *Sensors and Measuring Systems*; 21*th ITG*/*GMA-Symposium*, Nuremberg, 10-11 May 2022, 1-8.

[20] Lee, W.K., Schubert, M.J.W., Ooi, B.Y. and Ho, S.J.Q. (2018) Multi-Source Energy Harvesting and Storage for Floating Wireless Sensor Network Nodes with Long Range Communication Capability. *IEEE Transactions on Industry Applications*, **54**, 2606-2615. https://doi.org/10.1109/TIA.2018.2799158

[21] Paterova, T., Prauzek, M., Konecny, J., Ozana, S., Zmij, P., Stankus, M., Weise, D. and Pierer, A. (2021) Environment-Monitoring IoT Devices Powered by a TEG Which Converts Thermal Flux between Air and Near-Surface Soil into Electrical Energy. *Sensors*, **21**, Article 8098. https://doi.org/10.3390/s21238098

[22] Nakagawa, K. and Suzuki, T. (2016) A High-Efficiency Thermoelectric Module with Phase Change Material for IoT Power Supply. *Procedia Engineering*, **168**, 1630-1633. https://doi.org/10.1016/j.proeng.2016.11.477

[23] Kim Tuoi, T.T., Van Toan, N. and Ono, T. (2021) Heat Storage Thermoelectric Generator for Wireless IOT Sensing Systems. 2021 21*st International Conference on Solid-State Sensors*, *Actuators and Microsystems* (*Transducers*), Orlando, 20-24 June

2021, 924-927. https://doi.org/10.1109/Transducers50396.2021.9495686

[24] Mehne, P., Lickert, F., Bäumker, E., Kroener, M. and Woias, P. (2016) Energy-Autonomous Wireless Sensor Nodes for Automotive Applications, Powered by Thermoelectric Energy Harvesting. *Journal of Physics*: *Conference Series*, **773**, Article ID: 012041. https://doi.org/10.1088/1742-6596/773/1/012041

[25] Usón, S., Royo, J. and Canalís, P. (2023) Integration of Thermoelectric Generators in a Biomass Boiler: Experimental Tests and Study of Ash Deposition Effect. *Renewable Energy*, **214**, 395-406. https://doi.org/10.1016/j.renene.2023.05.100

[26] Najjar, Y.S.H. and Kseibi, M. (2017) Evaluation of Experimental JUST Thermoelectric Stove for Electricity—Deprived Regions. *Renewable and Sustainable Energy Reviews*, **69**, 854-861. https://doi.org/10.1016/j.rser.2016.07.041

[27] Jouhara, H., Żabnieńska-Góra, A., Khordehgah, N., Doraghi, Q., Ahmad, L., Norman, L., Axcell, B., Wrobel, L. and Dai, S. (2021) Thermoelectric Generator (TEG) Technologies and Applications. *International Journal of Thermofluids*, **9**, Article ID: 100063. https://doi.org/10.1016/j.ijft.2021.100063

[28] Jaziri, N., Boughamoura, A., Müller, J., Mezghani, B., Tounsi, F. and Ismail, M. (2020) A Comprehensive Review of Thermoelectric Generators: Technologies and Common Applications. *Energy Reports*, **6**, 264-287. https://doi.org/10.1016/j.egyr.2019.12.011

[29] Fernández-Yáñez, P., Gómez, A., García-Contreras, R. and Armas, O. (2018) Evaluating Thermoelectric Modules in Diesel Exhaust Systems: Potential under Urban and Extra-Urban Driving Conditions. *Journal of Cleaner Production*, **182**, 1070-1079. https://doi.org/10.1016/j.jclepro.2018.02.006

[30] Apertet, Y., Ouerdane, H., Goupil, C. and Lecœur, P. (2012) Internal Convection in Thermoelectric Generator Models. *Journal of Physics*: *Conference Series*, **395**, Article ID: 012103. https://doi.org/10.1088/1742-6596/395/1/012103

[31] EURECA (2023) Thermoelectric Generators. https://www.eureca.de/files/pdf/cooling/teg/TEGenerators.pdf

[32] Freunek, M., Müller, M., Ungan, T., Walker, W. and Reindl, L.M. (2009) New Physical Model for Thermoelectric Generators. *Journal of Electronic Materials*, **38**, 1214-1220. https://doi.org/10.1007/s11664-009-0665-y

[33] Durand-Estebe, P. (2016) Energy Recovery Systems for the Supply of Autonomous Sensors for Aeronautics. Master's Thesis, INSA Toulouse, Toulouse. https://www.theses.fr/2016ISAT0033

[34] (2023) Thermogenerator. https://shop.eureca.de/thermoelectric/seebeck-elements/413/teg1-30-30-8.5/200

[35] Wang, C.C., Hung, C.I. and Chen, W.H. (2012) Design of Heat Sink for Improving the Performance of Thermoelectric Generator Using Two-Stage Optimization. *Energy*, **39**, 236-245. https://doi.org/10.1016/j.energy.2012.01.025

[36] (2023) Cooling Element. https://coolinnovations.com/datasheets/3-2020XXM.pdf

[37] (2023) Magnet. https://www.kipp.fr/xs_db/DOKUMENT_DB/www/KIPP_DE_CH_PL/BEDIENTEILE/DataSheet/fr/K05/K0550_Datasheet_12598_Aimant_plat_en_SmCo--fr.pdf

[38] Nour Eddine, A. (2017) Modeling and Optimization of Waste Heat Recovery System Using the Thermoelectricity (Seebeck Effect) for Marine Application. Master's Thesis, Ecole centrale de Nantes, Nantes. https://www.theses.fr/2017ECDN0029

[39] Texas Instruments (2022) Ultra Low Power Boost Converter with Battery Management for Energy Harvester.

https://www.ti.com/product/BQ25504?utm_source=google&utm_medium=cpc&utm_campaign=app-null-null-GPN_EN-cpc-pf-google-eu&utm_content=BQ25504&ds_k=BQ25504&DCM=yes&gclid=EAIaIQobChMIkICNx_zf_QIVRgsGAB2qugLoEAAYASAAEgKCXvD_BwE&gclsrc=aw.ds

[40] Texas Instruments (2020) Ultra Low Power Harvester Power Management IC with Boost Charger, and Nanopower Buck Converter. https://www.ti.com/product/BQ25570?utm_source=google&utm_medium=cpc&utm_campaign=app-null-null-GPN_EN-cpc-pf-google-eu&utm_content=BQ25570&ds_k=BQ25570&DCM=yes&gclid=EAIaIQobChMI7Nut_vzf_QIVwrHtCh09SA91EAAYAyAAEgLi_vD_BwE&gclsrc=aw.ds

[41] (2020) Ultra Low Power Energy Harvester and Battery Charger with Embedded MPPT and LDOs. https://www.st.com/en/power-management/spv1050.html

[42] (2020) Energy-Harvesting Charger and Protector. https://www.analog.com/media/en/technical-documentation/data-sheets/max17710.pdf

[43] Analog Devices, Inc. (2021) Ultralow Power Boost Regulator with MPPT and Charge Management. https://www.analog.com/en/products/adp5090.html

[44] Singha Roy, P.K., Karayaka, H.B., He, J. and Yu, Y.H. (2021) Economic Comparison between Battery and Supercapacitor for Hourly Dispatching Wave Energy Converter Power. 2020 52*nd North American Power Symposium* (*NAPS*), Tempe, 11-13 April 2021, 1-6. https://doi.org/10.1109/NAPS50074.2021.9449677

[45] (2023) Supercapacitor Cell. https://www.farnell.com/datasheets/2849565.pdf

[46] Texas Instruments (2022) Synchronous Boost Converter with Ultra-Low Quiescent Current. https://www.ti.com/lit/ds/symlink/tps61099.pdf?ts=1678888228897&ref_url=https%253A%252F%252Fwww.ti.com%252Fproduct%252FTPS61099%253Futm_source%253Dgoogle%2526utm_medium%253Dcpc%2526utm_campaign%253Dapp-null-null-gpn_en-cpc-pf-google-wwe%2526utm_content%253Dtps61099%2526ds_k%253DTPS61099%2526dcm%253Dyes%2526gclid%253DCj0KCQjw2cWgBhDYARIsALggUhpadNWfPRGLOf-KRocS7hgMDSmy1QO_MBgkYAX4WdD2Z_L1yF3jbf2QaAgloEALw_wcB%2526gclsrc%253Daw.ds

[47] Texas Instruments (2023) Current Low-Dropout Linear Regulators in SC70 Package. https://www.ti.com/lit/ds/symlink/tps715-q1.pdf?ts=1679390231564&ref_url=https%253A%252F%252Fwww.google.com%252F

[48] (2023) DC Power Analyzer. https://www.keysight.com/us/en/product/N6705B/dc-power-analyzer-modular-600-w-4-slots.html

[49] Boitier, V., Tajan, P. and Dilhac, J.M. (2016) WSN Nodes: Design Considerations and Energy Management. *Journal of Physics*: *Conference Series*, **773**, Article ID: 012043. http://toc.proceedings.com/33294webtoc.pdf https://doi.org/10.1088/1742-6596/773/1/012043